

Specifics of Thermal Transport in Graphene Composites: The Effect of Lateral Dimensions of Graphene Fillers

Sriharsha Sudhindra^{1,2}, Farnia Rashvand³, Dylan Wright^{1,2}, Zahra Barani^{1,2}, Aleksey Drozdov⁴, Saba Baraghani^{1,5}, Claudia Backes³, Fariborz Kargar^{1,2,5,*}, and Alexander A. Balandin^{1,2}

¹Phonon Optimized Engineered Materials Center, University of California, Riverside, California 92521 USA

²Department of Electrical and Computer Engineering, Bourns College of Engineering, University of California, Riverside, California 92521 USA

³Institute of Physical Chemistry, Heidelberg University, Im Neuenheimer Feld 253, Heidelberg 69120 Germany

⁴Department of Materials and Production, Aalborg University, Fibigerstraede 16, Aalborg 9220 Denmark

⁵Department of Chemical and Environmental Engineering, University of California, Riverside, California 92521 USA

* Corresponding author: fkargar@ece.ucr.edu; web-site: <http://balandingroup.ucr.edu/>

Abstract

We report on the investigation of thermal transport in non-cured silicone composites with graphene fillers of different lateral dimensions. Graphene fillers are comprised of few-layer graphene flakes with lateral sizes in the range from 400 nm to 1200 nm and number of atomic planes from one to ~ 100 . The distribution of the lateral dimensions and thicknesses of graphene fillers has been determined *via* atomic force microscopy statistics. It was found that in the examined range of the lateral dimensions the thermal conductivity of the composites increases with the increasing size of the graphene fillers. The observed difference in thermal properties can be related to the average *gray* phonon mean free path in graphene, which has been estimated to be around ~ 800 nm at room temperature. The thermal contact resistance of composites with graphene fillers of 1200-nm lateral dimensions was also smaller than that of composites with graphene fillers of 400-nm lateral dimensions. The effects of the filler loading fraction and the filler size on the thermal conductivity of the composites were rationalized within the Kanari model. The obtained results are important for optimization of graphene fillers for applications in thermal interface materials for heat removal from high-power-density electronics.

Keywords: Thermal conductivity, contact resistance, graphene, composites, thermal interface materials, power electronics

I. Introduction

The exfoliation and electrical experiments with graphene¹ motivated studies of other properties of this material, and led to the discovery of unique thermal conductivity of graphene and few-layer graphene (FLG)^{2–6}. In recent years, one can witness a transition of graphene and FLG to numerous practical applications, which utilize their thermal properties, including composite coatings, solid heat spreaders and thermal interface materials (TIMs)^{7–21}. The use of graphene – FLG mixture as fillers in composites proved to be particularly beneficial. The initial studies found that the thermal conductivity of epoxy-based composites with low loading fractions of randomly distributed graphene fillers can be improved substantially by a factor of $\times 25$ ^{7,22}. Similar significant enhancement in the thermal conductivity characteristics of non-cured TIMs with graphene fillers has been reported by us and others as well [X-X]. The comparative study on the thermal conductivity of graphene-based non-cured TIMs with those of commercially available ones with fillers other than graphene shows that the former transfer heats more effectively even with lower filler inclusion¹⁴. Reports from different research groups confirmed the potential of graphene fillers for thermal management applications (for comprehensive reviews on the topic see Ref. ^{23–25}). There is a general consensus that unique heat conduction properties of single-layer graphene (SLG) and FLG are the enablers of such applications^{2,6}. Here and below, we adopt a convention that in the thermal context the term “*graphene fillers*” means a blend of SLG and FLG.

Almost all studies of TIMs with graphene fillers are focused on the thermal conductivity and thermal diffusivity values of the resulting composites as the functions of the graphene loading fraction^{23–25}. Several studies addressed the issues of the thermal percolation threshold^{15,26} and “synergistic” effects^{12,27–30}. In the context of various TIMs, it was established that the percolation threshold depends on the filler sizes^{31–33}. The existence and the strength of the “synergistic” effect, *i.e.*, the additional enhancement of the thermal conductivity when a single type of filler with different sizes or two or more filler materials are used, is also known to depend on the size and aspect ratio of the fillers. Despite the importance of the knowledge of how the lateral dimensions of graphene fillers affect the thermal conductivity of the composites, there have been a limited number of studies on this subject^{26,34,35}. We are not aware of any reports on the effect of the graphene filler size on the thermal contact resistance of TIMs at the interfaces with solid surfaces. Possible reasons for the lack of such data are the challenges in the preparation of consistent set of

samples with different and quantifiable average lateral size of fillers when prepared in large quantities required for TIM preparations.

Investigation of thermal transport properties of composites with graphene and FLG fillers that have different lateral dimensions is important for industrial applications and meanwhile from the fundamental science aspects. We hypothesize that graphene fillers with lateral dimensions exceeding the phonon mean free path (MFP) preserve their high intrinsic thermal properties by limiting the effect of phonon – edge scattering. From the other side, the fillers with excessively large lateral dimensions can be technologically impractical owing to the strong bending of the fillers and increased bond line thickness, *BLT*. There are other factors, related to the lateral size of the fillers, which can affect the heat conduction in the composites. They include the Kapitza resistance between the fillers and matrix material ³⁶, the specific surface area, interface area between the filler and matrix ^{37–41}, and the defect density ^{4,42–44}. The above considerations motivated us to investigate the specifics of heat conduction in TIMs with graphene fillers where the lateral dimensions of the fillers are below, close, or above graphene's gray phonon MFP. A particular emphasis of the study was on selecting a proper sample set with the well-defined average lateral dimensions of the fillers, systematic analysis of the filler size distribution, and accurate thermal measurements following the standard techniques used in industry for TIM performance characterization. In order to understand the effect of the filler size, we intentionally used low loading of the graphene fillers, kept the dimensions as uniform as possible, and selected the lateral dimensions of the fillers relatively small, *i.e.*, close to the gray phonon MFP. For the above reasons, the resulting values of the thermal conductivity of the studied composites were not high. Thermal transport across the interface between the composite and the solid surface was another component of this research. The latter has practical importance for application of graphene TIMs for thermal management of power electronics.

II. Experimental Procedures

In this study, different sets of non-cured TIMs with base polymer of silicone oil and inclusions of graphene and FLG fillers were prepared. The fillers were produced from graphite using the liquid phase exfoliation (LPE) technique ^{45–49} in aqueous surfactant solution in combination with liquid

cascade centrifugation^{50,51} for size selection. This allowed us to produce three fractions from the same stock dispersion with different lateral size and thickness distributions. The exfoliated graphene fillers were extracted from the solvent and incorporated within the base polymer to produce the required composites. The details of the exfoliation and composite preparation are outlined in the METHODS. The fillers were characterized for lateral dimension and thickness, *i.e.*, number of layers, using atomic force microscopy (AFM) and optical extinction spectroscopy to assess the concentration/mass. In Figure 1, we present the AFM characterization data for the three size-selected sets of fillers. Figure 1 (a-c) shows the two-dimensional images of the dispersed graphene fillers in the size-selected fractions. The procedure used to assess the average dimensions is outlined in the METHODS. The resultant histograms for the longest dimension of the fillers (termed length, L) are given in Figure 1 (d-f) while the histograms for the number of atomic planes, N , are given in Figure 1 (g-i). Note that due to the lognormal shape of the distributions, there are different ways to describe the average. Here, we focus on the arithmetic mean of the filler dimensions which were 1200 nm, 800 nm and 400 nm in the case of the longest dimension, while the average number of atomic planes were determined to be 40, 19 and 8. For simplicity, we label these fillers as “large”, “medium” and “small,” respectively. Additional characterization data for the graphene fillers, *i.e.*, scanning electron microscopy (SEM) and optical extinction spectroscopy are provided in the Supplementary Information.

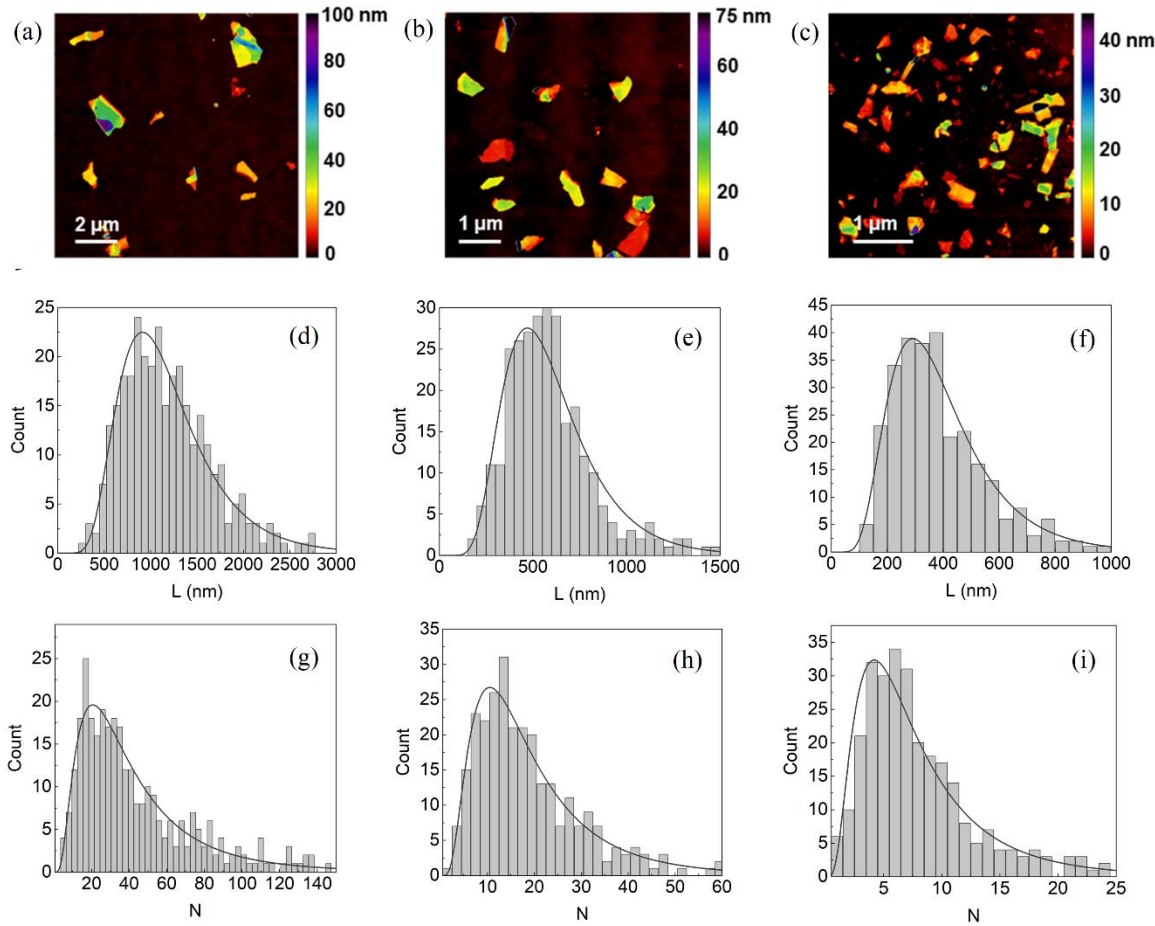


[Figure 1: Characterization of lateral dimensions of graphene fillers. (a–c) AFM images of the large (1200 nm), medium (800 nm) and small (400 nm) size fillers, respectively after drop-casting the dispersions on Si/SiO₂. (d–f) Histograms of the measured filler lengths used for determining three groups of the filler sizes. (g–i) Histograms of the number of atomic planes in the three groups of the fillers. Note that the large fillers have lateral dimensions near or exceeding the gray phonon MFP in graphene.]

It is important to note that there exists a specific correlation between the number of atomic planes in FLG and its lateral dimensions. One cannot obtain FLG fillers with a fixed number of atomic planes and different lateral dimensions. This is related to details of the exfoliation mechanism which can be understood in terms of delamination accompanied with tearing⁵². The centrifugation, which is required for the size selection, enhances this correlation and typically produces small fillers that are thinner and large fillers that are thicker^{50–52}. This correlation can be illustrated *via* a plot of the filler area as function of number of the atomic planes. Figure 2 (a) shows the measure of the characteristic lateral length, $L_* = (L \times W)^{0.5}$ vs. the number of atomic planes, N (here L

and W are the measured “length” and “width” of the fillers from AFM). In this plot, each data point corresponds to a single graphene sheet measured with AFM in the size-selected fractions. The exact specification of the fillers obtained from AFM data are summarized in Table 1. For FLG, the lateral dimensions affect the thermal transport stronger than the thickness ^{23–25,53–58}. For this reason, the synthesized three sets of composite samples are meaningful for understanding the specifics heat conduction and the effects of the filler size.

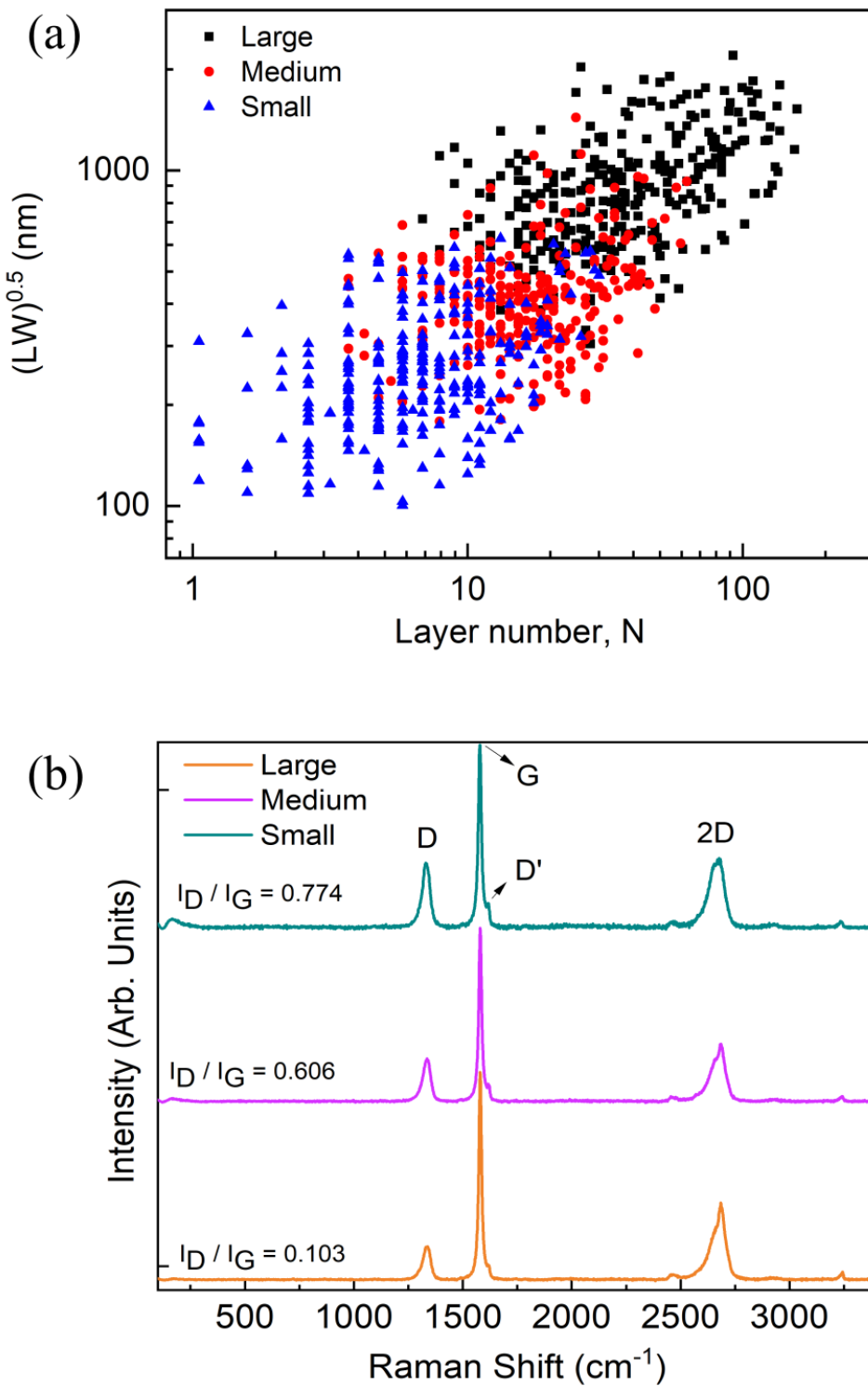


[Figure 2: (a) Correlation between the measure of the lateral dimensions of the fillers and the number of the atomic planes. The numerous data points denote the multiple measurements conducted with AFM. (b) Raman spectra of the graphene fillers of different lateral dimensions.]

We have verified the quality of fillers using Raman spectroscopy (Renishaw inVia). Figure 2 (b) shows the measured Raman spectra of the size-selected graphene samples used in this study. To conduct the tests, a small portion of the fillers were transferred onto a Si/SiO₂ substrate. The light scattering spectra were collected under a laser excitation of the wavelength 633 nm (red) and an excitation power of 2 mW at room temperature. The Raman spectra show well-known signatures of FLG, which are the G peak and 2D band^{51,54,55,59–61}. As expected, the intensity of the disorder D peak increases as the size of the fillers decrease. These evolution of the peaks with the lateral dimensions and the number of the atomic planes is in line with prior literature reports^{59,60,62–64}. The I_D/I_G ratio is correlated with the difference in the average size of the fillers⁶⁵. The I_D/I_G ratio decreases as the size of the fillers increases, changing from 0.774 for the small fillers to 0.103 for the large fillers. The evolution of the D peak and I_D/I_G can be explained by the relaxation of the selection rules, which prohibit the appearance of the D peak in graphene with perfect translation symmetry, without defects or edges^{66,67}. In the samples with smaller graphene fillers, the excitation laser light covers more graphene fillers with the edges that act as inherent defects thus resulting in an increased I_D/I_G ratio. The 2D peak becomes more symmetric with decreasing dimensions of the fillers which is in this case related to change in the number of atomic planes. However, as outlined recently, this cannot be used as quantitative measure for thickness in LPE graphene⁶⁸. A comparison of the I_D/I_G ratios with the AFM acquired characteristics of the graphene fillers is presented in the Supplementary Information.

Table 1: Characteristics of Graphene – FLG Fillers.

	Symbol	Large	Medium	Small
Average length (nm)	<i>L</i>	1200	600	400
Aspect ratio (length/width)	<i>L/W</i>	1.8	2.1	2.3
Aspect ratio (length/thickness)	<i>(L/t)</i>	110	120	200
Average layer number	<i>N</i>	40	19	8
Characteristic length (<i>L</i> × <i>W</i>) ^{0.5} (nm)	<i>L_*</i>	900	430	270

The total thermal resistance, *R_{tot}*, bulk thermal conductivity, and thermal contact resistance, *R_C*, of the TIMs with the steel plates were measured using an industrial TIM tester (LongWin Science and Technology Corp.). The instrument operates based on the procedures and regulations described in the standard ASTM D5470⁶⁹. The prepared TIMs were tested for their thermal

properties by applying them between two finely polished steel plates available within the equipment. These two plates are the heat source and heat sink and their roughness is in the nm range. The thermal performance of the TIM at the interface is tested by carefully measuring the heat flow transferring from the source to the heat sink and measuring the temperature gradient formed across the TIM layer.¹⁷ Assuming a one-dimensional heat flow, the apparent thermal conductivity of the TIMs can be calculated by solving the one-dimensional Fourier heat transport equation. The total thermal resistance from our measurements can be defined as^{7,70,71}:

$$R_{tot} = \frac{BLT}{K_{TIM}} + R_{C1} + R_{C2} \quad (1)$$

Where, K_{TIM} , R_{C1} , and R_{C2} are the thermal conductivity if the TIM and the thermal contact resistances of the TIM with the two plates present in the measurement equipment, respectively. The measurements were carried out on TIMs with graphene of three filler sizes at multiple loading fractions while utilizing standard plastic shims to obtain measurements at different controlled BLTs. All measurements have been performed under an applied pressure of $P = 0.55$ MPa (~80 psi). Further details of the thermal testing are provided in the METHODS.

III. Results and Discussion

The total thermal resistance, R_{tot} , of the prepared non-cured graphene composites as a function of BLT is presented in Figure 3(a-c). The data are shown for all three lateral dimensions of the graphene fillers at different loading fractions, f . The acquired data were fitted using the least squares linear regression line at each loading fraction and for each size of graphene fillers. The bulk thermal conductivity of each TIM was then obtained from the inverse of the regression slope, K_{TIM} ($\text{Wm}^{-1}\text{K}^{-1}$) = $(1/\text{Slope}) \times 100$. The total thermal contact resistance, $2R_C$, assuming that $R_{C1} = R_{C2} = R_C$ were acquired from the y -intercepts of the fittings. One can see that the thermal resistance at constant thickness is the highest for the pure matrix material, *i.e.*, silicone oil, without the graphene addition while being the lowest for the composites with the higher loading fraction of graphene. However, it is difficult to make conclusions about the effect of the filler size

from this plot. The latter can be done in a meaningful way from the analysis of the thermal conductivity and thermal contact resistance.

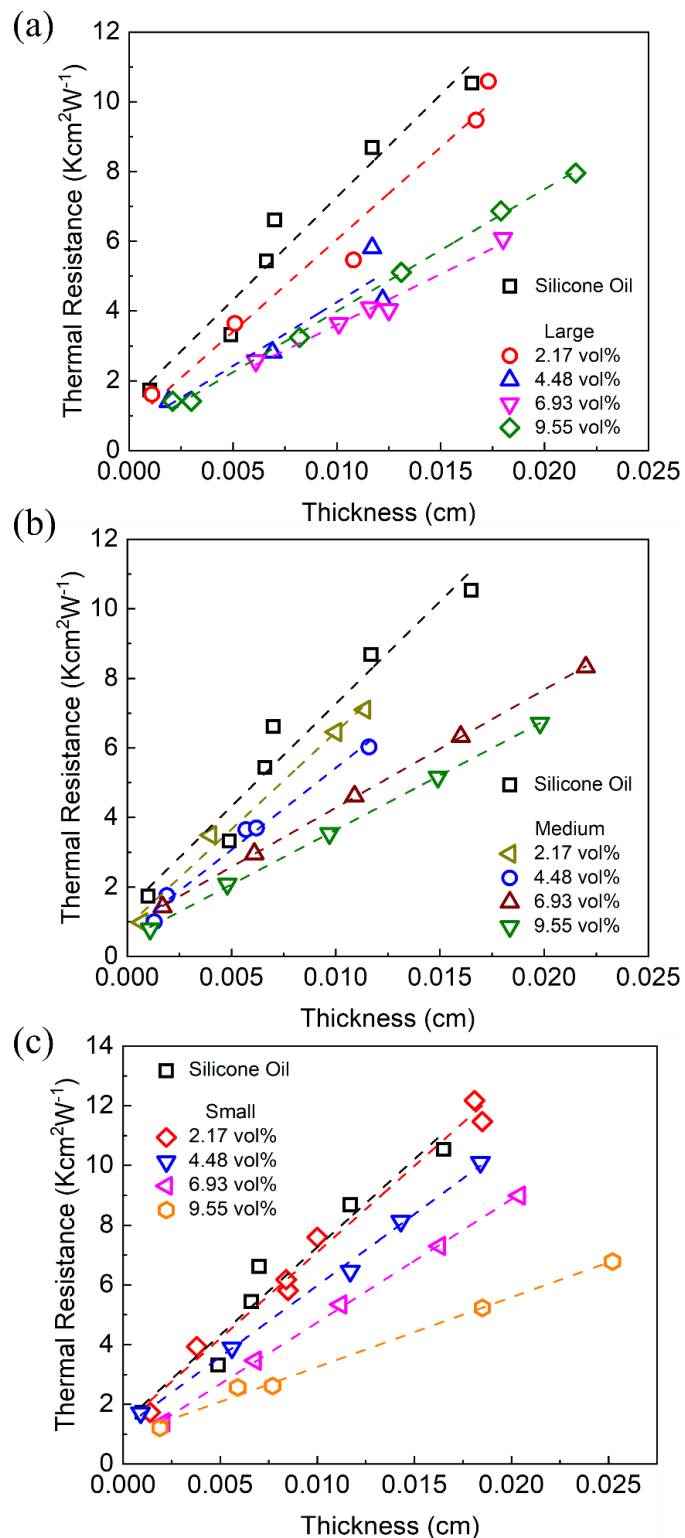


[Figure 3: Total thermal resistance of the TIMs with (a) large, (b) medium, and (c) small graphene fillers as a function of the TIM's bond line thickness. The slope and y-intercept of the fitted dashed lines were used to calculate the thermal conductivity and thermal contact resistance of each set.]

Figure 4 shows the thermal contact resistance, R_C , as a function of graphene loading fraction for three examined graphene filler sizes. The thermal contact resistance is the smallest for the graphene fillers with the largest lateral dimensions and decreases with increasing filler loading fraction. The dependency of the thermal contact resistance on the filler loading and lateral dimensions can be interpreted with the help of the following semi-empirical model^{72,73}:

$$R_{C_1+C_2} = 2R_C = c \left(\frac{\zeta}{k_{TIM}} \right) \left(\frac{G}{P} \right)^n. \quad (2)$$

In Eq. (2), $G = \sqrt{G'^2 + G''^2}$ is a function of the storage (G') and loss shear modulus (G'') of the TIM. ζ and P are the surface roughness of the binding steel plates and the applied pressure in the experiments and c and n are empirical coefficients. There are two competing parameters, k_{TIM} and G , in this equation as fillers are introduced eventually to the polymer. Both these parameters, irrespective of the size of the fillers, increase with addition of fillers. However, G' and G'' strongly depend on the filler size. at constant filler inclusion, the smaller the filler size, the higher the values of G' and G'' and thus, G [Refs. 77–84]. That is why in Figure 4, keeping ζ and P , smaller graphene fillers exhibit the highest thermal contact resistance. On a closer look, one can say that Eq. (2) would suggest that for TIMs with a specific filler, graphene fillers of varying filler dimensions in this case, there would exist an ideal loading of fillers at which there would be a significant increase in k_{TIM} , which would slightly affect the performance of R_C . This realization would appear more evident when Eq. (2) is incorporated into Eq. (1) and restated as:

$$R_{tot} = \left(\frac{1}{k_{TIM}} \right) \left\{ BLT + c\zeta \left(\frac{G}{P} \right)^n \right\}. \quad (3)$$

Eq. (3) shows confirms the importance of increasing the TIM bulk thermal conductivity as it contributes to decrease the thermal resistance of the TIM layer as well as the thermal contact resistance, and thus the total thermal resistance. Rheological properties of non-cured TIMs and their variation with pressure and temperature have important implications in practical applications

mostly related to pump-out issues ^{14,74–76}. It is generally suggested that in order to avoid the issue of pump-out, G' of non-cured TIMs should be greater than G'' [Ref. ⁷³].

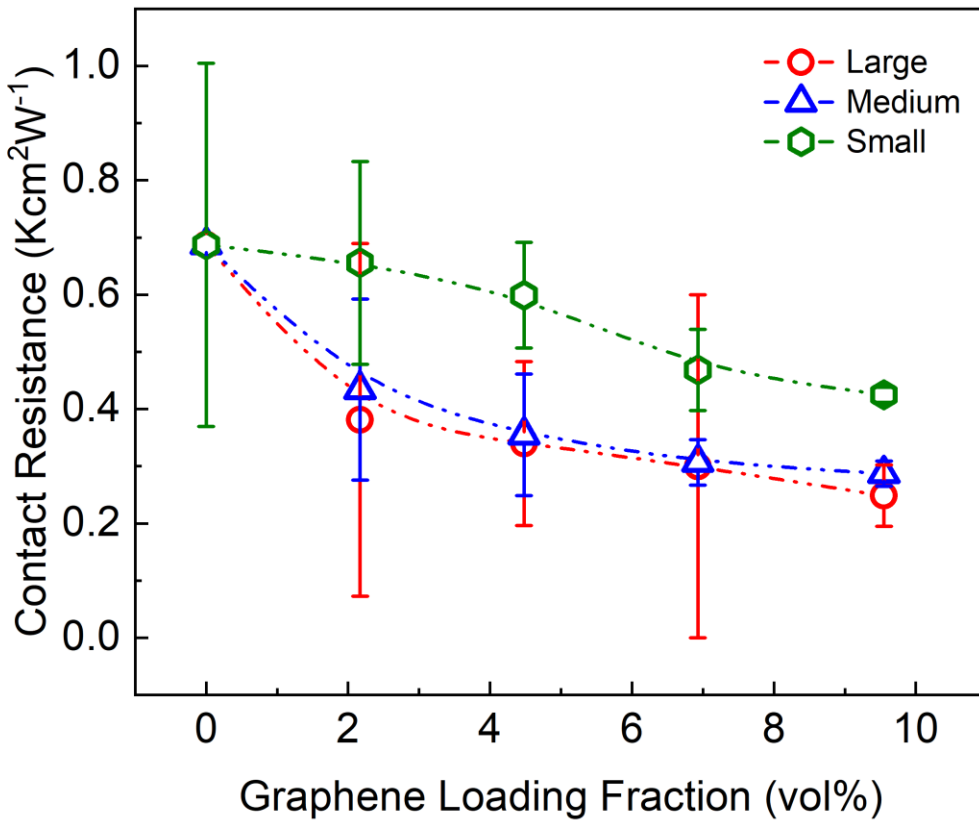


[Figure 4: Contact resistance of the TIMs as a function of the graphene filler loading fraction. The error bars show the standard associated with the linear regressions over experimental data. The dashed lines are shown as guides to the eye.]

In Figure 5, the symbols show the extracted experimental thermal conductivity as a function of graphene loading fraction for three examined graphene filler sizes and its comparison with theoretical modelling (dashed lines). The measured thermal conductivity of the base polymer matrix – silicone oil was $0.17 \text{ Wm}^{-1}\text{K}^{-1}$ which agrees with the previously reported values ^{17,86–88}. The thermal conductivity is higher for the large filler size TIMs at all the measured loading fractions. We rationalize this trend by comparing the size of the graphene fillers with the average,

also referred to as *gray* phonon MFP in graphene. The gray phonon MFP in graphene is reported to be ~ 800 nm at RT^{53–58,89}. The improvement in the thermal conductivity of the TIMs originates from the partial contribution of thermal transport via the graphene fillers. If the filler lateral dimensions become smaller than the phonon MFP its intrinsic thermal conductivity decreases. The simple estimate comes from the Debye model, where the thermal conductivity $K \sim C\nu\Lambda$ (here, C is the volumetric specific heat, ν is the average phonon group velocity and Λ is the average phonon MFP). When the size of the filler $L < \Lambda$, the thermal conductivity, K , scales down linearly with lateral dimension, L . This explanation remains valid for the thermal transport regime below and above the thermal percolation threshold¹⁵.

One should also note that the measured values of thermal conductivity of the examined TIMs are not high. The goal of the present study was not achieving the highest thermal conductivity but rather a systematic study of the effect of the filler size on TIM's thermal transport characteristics. For this reason, we used low loading of graphene fillers, which allowed us to avoid agglomeration and viscosity increase; relatively small size of the fillers, close to the gray phonon MFP; and the fillers of the same size within each batch. In order to obtain the highest possible values of the thermal conductivity with graphene fillers, one would need to use higher loading fractions of the fillers; select the fillers with larger average lateral dimensions; prepare a mixture of fillers with different sizes to achieve the synergistic effect; and functionalize the fillers for better coupling to the matrix. We have reported strategies for maximizing the enhancement of the thermal conductivity of graphene curing and non-curing composites and TIMs elsewhere^{12,14,15}. One should note that the low loading of graphene fillers with non-curing base material allowed us to minimize the problems associated with the high viscosity of composites at higher loadings. The viscosity of the composites depends on the filler loading and filler size distribution. The viscosity also affects the “pump-out” in non-cured TIMs. These secondary effects go beyond the scope of the present work and will be addressed in a separate study.

We employed the theoretical model of Kanari⁹⁰ to investigate the effect of filler content and its characteristics dimensions on the thermal conductivity of the polymer TIMs shown in Figure 5 .

This model was originally introduced as an empirical extension of the Bruggerman relation⁹¹. The derivation of the Kanari model within the micromechanical framework was described in details previously⁹². According to this approach, thermal conductivity, K_{TIM} , of a composite consisting of a polymer matrix laden with particles of an arbitrary shape is determined by the equation:

$$\frac{k_f - K_{TIM}}{k_f - k_m} \left(\frac{k_m}{K_{TIM}} \right)^{\frac{1}{B}} = 1 - f, \quad (4)$$

in which k_m and k_f are the thermal conductivities of the matrix and filler, respectively, f is the filler volume fraction, and B is a parameter characterizing shape of the filler particles. We treat these inclusions (stacks of graphene plates) as oblate ellipsoids of rotation with semi-axes $a_1 < a_2 = a_3$, where a_1 denotes the characteristic thickness of a stack, and $a_2 = a_3 = L_*$ stands for its in-plane size. Under this condition and given that $k_f \gg k_m$, the coefficient B reads

$$B = \frac{4 - 3M}{3M(1 - M)} \quad (5)$$

with

$$M = \frac{2\varphi - \sin \varphi}{2\sin^2 \varphi} \cos \varphi, \quad \cos \varphi = \frac{a_1}{a_2} \quad (6)$$

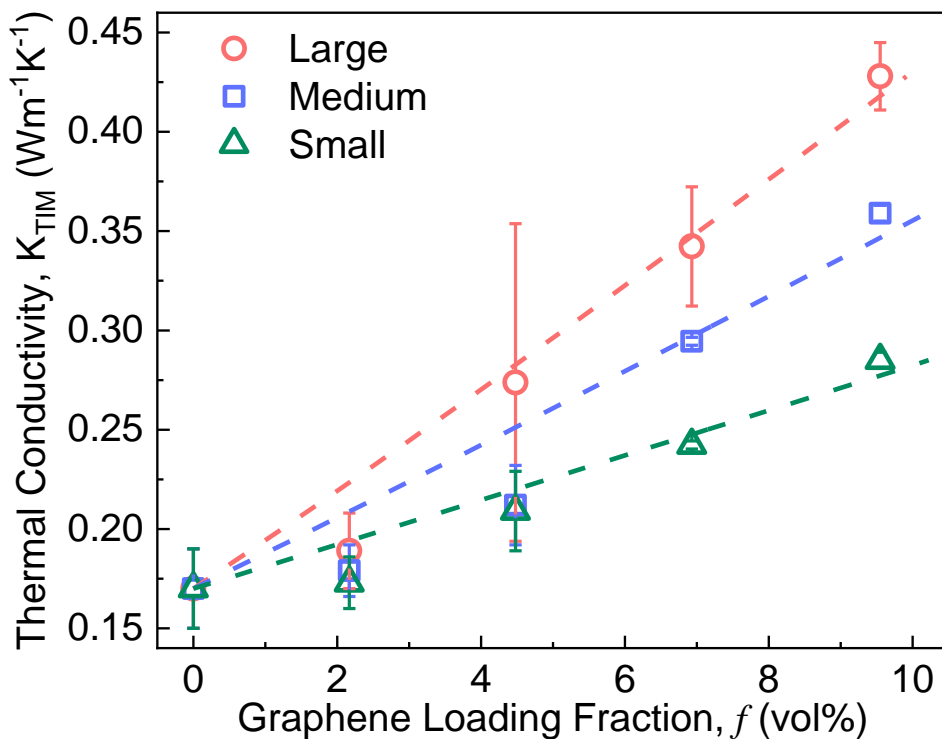


[**Figure 5:** Experimentally acquired thermal conductivity (symbols) of the non-cured TIMs as a function of the graphene loading fraction, f , for three different sizes of the fillers with comparison to Kanari model (dashed lines).]

Figure 5 demonstrates reasonable agreement between the experimental data of composites with stacks of small, medium and large graphene fillers and predictions of Eq. (4). Each set of data is matched separately by means of the only parameter: the effective thermal conductivity of stacks k_f . In simulation, we adopt the value $k_m = 0.17 \text{ Wm}^{-1}\text{K}^{-1}$ for thermal conductivity of the matrix. The coefficients φ , M , and B , related to the aspect ratio of stacks, are calculated based on the experimental characterization of the fillers (Table 1) and their values are summarized in Table 2. The experimentally obtained set of data for TIMs with large, medium and small size graphene fillers have been presented in the supplementary document.

Table 2: Parameters of the Kanari model for Graphene Composites

Filler Type	Layer Number (N)	thickness (a_1)[nm]	Plane dimension ($a_2 = a_3 = L_*$)[nm]	ϕ [rad]	M	B
Large	40	14	900	1.5552	0.0164	81.5419
Medium	19	6.65	430	1.55533	0.0163	82.0100
Small	8	2.8	270	1.56043	0.0110	121.5660

The effect of the in-plane size of fillers on their effective thermal conductivity k_f is illustrated in Figure 6. In this figure, the k_f is plotted versus L_* together with approximation of the data by an exponential function

$$k_f = k_f^0 + k_f^1 \exp(-\alpha L_*), \quad (7)$$

where $k_f^0 = 3.32$, $k_f^1 = -4.83$, and $\alpha = 0.0033$ are fitting parameters. Figure 6 shows that k_f increases by a factor of 2.2 with L_* when the in-plane size of the fillers grows from 270 to 900 nm. The extracted effective thermal conductivity of fillers is orders of magnitude smaller than the intrinsic thermal conductivity of graphene due to the filler-polymer thermal boundary resistance. However, the decrease in the effective thermal conductivity of the fillers as their size shrinks below graphene's phonon MFP is originated from a strong suppression of the its intrinsic thermal conductivity due to the enhanced phonon-edge scattering.

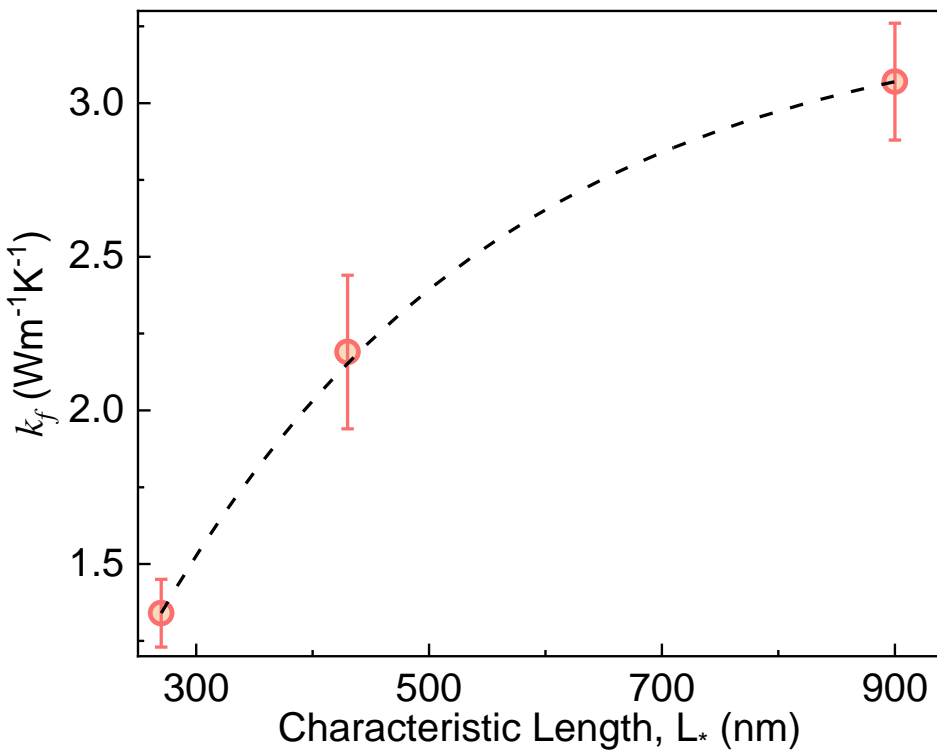


[Figure 6: Effective thermal conductivity of filler k_f versus the characteristic in-plane size of graphene fillers L_* .]

Our present detailed systematic study proves that a stronger enhancement of the thermal conductivity of graphene composites can be achieved when the fillers with larger lateral dimensions are used. This conclusion is in line with our own early observation ⁹³, and a few other reports that were performed with different graphene filler sizes ^{26,34,35,94,95}. The prior studies were focused on substantially larger fillers, with dimensions typically above 5 μm . In many cases, no accurate assessment and averaging were performed for the size distribution of the fillers. By selecting the average filler sizes near the phonon MFP in graphene, *i.e.*, slightly smaller, almost equal to MFP, and slightly larger, we were able to connect the observed trend with the intrinsic heat conduction properties of FLG. The observation that the thermal contact resistance also decreases with increasing the graphene filler size is non-obvious, and to some degree, it is counter-intuitive. The obtained trends shed light on the specifics of heat conduction in graphene composites, and can be used for optimization of graphene TIMs for practical applications.

IV. Conclusions

We reported on thermal properties of non-cured silicone composites with graphene fillers of different lateral dimensions. To elucidate the effect of the physical size of graphene fillers, we intentionally used low loading of graphene fillers to avoid agglomeration, used relatively small fillers, and kept the size uniform as much as possible. The studied graphene fillers were comprised of FLG flakes with lateral sizes in the range from 400 nm to 1200 nm and number of atomic planes from one to \sim 100. The physical characteristics of the graphene fillers were determined with AFM and verified with various characterization techniques. It was found that in the examined range of the lateral dimensions the thermal conductivity of the composites increases with the increasing size of the graphene fillers. The thermal contact resistance of composites with graphene fillers of 1200-nm lateral dimensions was also smaller than that of composites with graphene fillers of 400-nm lateral dimensions. The effects of the filler loading fraction and the filler size on the thermal conductivity of the composites were rationalized within the Kanari model. The obtained results are important for optimization of graphene fillers for applications in TIMs for heat removal from high-power-density electronics where the thermal resistance between the device and packaging is often a bottleneck impeding the heat removal. The high-power switches implemented with diamond and other wide-band-gap semiconductors are also often characterized by higher roughness on the surface allowing for the use of TIMs with larger fillers for enhanced performance.

METHODS

Liquid Phase Exfoliation: Preparation of graphene dispersions were achieved by probe sonication of the commercially acquired graphite powder (Sigma Aldrich 496596 in an aqueous solution of sodium cholate (SC) with an initial concentration of 40 gL^{-1} . The obtained powder was immersed in 80 mL of aqueous surfactant solution ($C_{\text{surf}} = 6 \text{ gL}^{-1}$) in a stainless-steel beaker and then subjected to a two-step sonication process. This step was carried out to remove the impurities present in the powder. In the first step: 1) The mixture was sonicated for a duration of 1 hour at a 60 % Amplitude in a 8 sec on, 2 sec off pulse sequence, with a Sonics Vibracell VCX 500 (500 W), equipped with

both a threaded probe and a replaceable tip. The dispersion was kept at 5 °C in a cryostat cooled water bath to avoid heating of the sample during the process of sonication. After the completion of the sonication process, the dispersion was centrifuged at 3800 g for 1.5 hours in a Hettich Mikro 220R centrifuge, equipped with a 1016 fixed-angle rotor at a temperature of 15 °C. The supernatant containing the water-soluble impurities was discarded and the sediment was re-dispersed in 80 ml of 2 gL⁻¹ aqueous surfactant solution. 2) This dispersion was then again sonicated for 5 hours at a 60 % Amplitude in a 6 sec on, 2 sec off pulse sequence.

In order to distinguish the acquired nanosheets by their size, we utilized the technique of liquid cascade centrifugation with sequentially increasing the rotation speeds (2 hours each step, with a temperature of 15°C). After each centrifugation step, the supernatant and sediment were separated, the sediment collected in reduced volume (~10 mL) and surfactant concentration (0.1 gL⁻¹) and the supernatant subjected to centrifugation at higher speeds. Here, relative centrifugal field (RCF) in units of the earth's gravitational force, *g* is used to describe the centrifugation conditions. Centrifugation was performed with a JA25.50 fixed angle rotor of a Beckman Coulter Avanti centrifuge at a temperature of 15°C for 2 hours with 50 mL centrifuge tubes (VWR, order number 525-0402) filled with 20 mL of each dispersion. The following RCF were used: 30, 200, 2500 g. The supernatant after 2500 g was discarded. The sediment after the centrifugation step at 30 g contains the largest sheets, but also unexfoliated bulk material. To separate the two, the dispersion was left to settle for 16 h and the top 80% of the volume decanted and collected. This sample is denoted as "large". "Medium" refers to the sample trapped between 30 and 200 g centrifugation, while "small" denotes the sample obtained from centrifugation between 200 and 2500 g. The exfoliation and size selection procedure were repeated 4 times to produce a sufficiently large mass of nanosheets. The same fractions of all batches were combined. In a final step, the filler was transferred to t-Butoxymethyl-oxiran as a solvent for better compatibility with the composite preparation. To this end, the combined fractions were centrifuged at 3000 g for 2 hours, the clear supernatant removed and the sediment re-dispersed in the solvent.

Characterization of Fillers: Optical extinction of the fillers were measured on a Varian Cary 6000i in quartz cuvettes with a pathlength of 1 cm in 0.5 nm increments and integration times of

0.1 s/nm. The obtained sediments after LCC were diluted with an aqueous surfactant solution containing (0.1 gL⁻¹) such that their optical densities after background subtraction were < 1. The extinction at 750 nm was multiplied with the dilution factor and the concentration determined using the reported size-independent extinction coefficient of 54.5 gL⁻¹cm⁻¹⁵¹. With knowledge of the total volume, the total mass of graphene in each sample was calculated. For AFM, the concentrated dispersions after size selection were diluted with de-ionized water to optical densities of ~1 and drop-cast on Si/SiO₂ wafers that were heated to ~150°C on a hotplate. This results in flash evaporation of the solvent to minimize aggregation on the substrate. For imaging, an aluminium coated silicon AFM cantilever and tip (OLTESPA-R3) was used with the Dimension ICON3 scanning probe microscope (Bruker AXS S.A.S.) in ScanAsyst mode (non-contact) in air under ambient conditions. Typical image sizes ranged from 20x20 μm² in the case of the largest sheets to 5x5 μm² for the sample containing the smaller sheets. The scanning parameters used were a pixel of 1024 lines with a scan rates of ~0.4 Hz and a peak force setpoints of ~0.1 V. Using Gwyddion software, the longest dimension (length), dimension perpendicular (width) and thickness of ~300 individually deposited nanosheets in each sample was manually measured. The acquired thickness was essential to obtain the layer number which was acquired using the previously reported step height of LPE graphene of 0.9 nm⁹⁶. The lateral dimensions were corrected for cantilever broadening and pixilation by using an empirical correction⁹⁷. From the distributions, the arithmetic averages of the dimensions were calculated. Due to the lognormal shape of the distributions, we note that the arithmetic average is larger than the maximum (i.e. the mode) of the distribution. To estimate the average length/thickness aspect ratio, the length of each sheet was divided by the layer number multiplied with the crystallographic thickness of one layer (0.35 nm) and the arithmetic mean calculated.

Composite Synthesis: The exfoliated graphene fillers were centrifuged with a solvent of t-Butoxymethyl-oxiran in a vial at 7000 rpm for 2 minutes to ensure that the fillers were visually separated from the solvent. The solvent was removed from the vial to an extent using a dropper and the remaining contents of the vial were transferred to a petri dish in a fume hood for 24 hours at room temperature. This enabled the solvent to completely evaporate leaving us with only the fillers. These extracted fillers were precalculated and added to the base polymer matrix of silicone

oil (Fisher Scientific, USA), also known as PDMS – Poly(dimethylsiloxane). The obtained compound was then shear mixed (Flacktek Inc.) at a speed of 2000 rpm for 10 minutes followed by a speed of 3000 rpm for 15 minutes to ensure homogenous distribution of the filler in the polymer. This process was repeated for all the filler sizes and with all loading fractions.

Thermal Characterization: The prepared composites were experimentally tested to acquire their thermal conductivity and contact resistance with the LW-9389 industrial ASTM-D5470 LongWin TIM tester (LongWin Science and Technology Corp, Taiwan). Experimental parameters with a pressure of 80 psi, temperature of 80 °C for a duration of 40 minutes for each data point were used for the non-cured composites with graphene fillers.

Supporting Information

Supporting Supplementary Information is available from the journal web-site for free of charge.

Acknowledgements

The work at UC Riverside was supported, in part, by ULTRA, an Energy Frontier Research Center (EFRC) funded by the U.S. Department of Energy, Office of Science, Basic Energy Sciences under Award # DE-SC0021230.

Contributions

F.K. and A.A.B. conceived the idea of the study and coordinated the project. S.S. prepared the thermal compounds, performed thermal conductivity measurements, thermal contact resistance measurements and conducted data analysis of thermal and Raman data; F.R. performed LPE, AFM and optical extinction measurements on the fillers and conducted analysis; D.W. assisted with thermal measurements and analysis; Z.B. performed Raman spectroscopy measurements and assisted in thermal compound preparation and analysis of Raman data; A.D performed modeling of the experimental data and compared them; F.K. contributed to the experimental and theoretical

data analysis; S.B. performed SEM of the graphene fillers; C.B. supervised LPE, AFM and optical absorption of the fillers and contributed to analysis; A.A.B. contributed to thermal and Raman data analyses; F.K. and A.A.B. led the manuscript preparation. All authors contributed to writing and editing of the manuscript.

ORCID

Sriharsha Sudhindra: 0000-0001-5299-3962

Dylan Wright: 0000-0001-5764-6003

Zahra Barani: 0000-0002-4850-0675

Aleksey Drozdov: 0000-0002-6049-5813

Saba Baraghani: 0000-0003-0256-0397

Claudia Backes: 0000-0002-4154-0439

Fariborz Kargar: 0000-0003-2192-2023

Alexander A. Balandin: 0000-0002-9944-7894

References

- (1) Novoselov, K. S.; Geim, A. K.; Morozov, S. v.; Jiang, D.; Zhang, Y.; Dubonos, S. v.; Grigorieva, I. v.; Firsov, A. A. Electric Field Effect in Atomically Thin Carbon Films. *Science* **2004**, *306* (5696), 666–669. <https://doi.org/10.1126/science.1102896>.
- (2) Balandin, A. A.; Ghosh, S.; Bao, W.; Calizo, I.; Teweldebrhan, D.; Miao, F.; Lau, C. N. Superior Thermal Conductivity of Single-Layer Graphene. *Nano Letters* **2008**, *8* (3), 902–907. <https://doi.org/10.1021/nl0731872>.
- (3) Ghosh, S.; Calizo, I.; Teweldebrhan, D.; Pokatilov, E. P.; Nika, D. L.; Balandin, A. A.; Bao, W.; Miao, F.; Lau, C. N. Extremely High Thermal Conductivity of Graphene: Prospects for

Thermal Management Applications in Nanoelectronic Circuits. *Applied Physics Letters* **2008**, *92* (15), 151911. <https://doi.org/10.1063/1.2907977>.

- (4) Ghosh, S.; Bao, W.; Nika, D. L.; Subrina, S.; Pokatilov, E. P.; Lau, C. N.; Balandin, A. A. Dimensional Crossover of Thermal Transport in Few-Layer Graphene. *Nature Materials* **2010**, *9* (7), 555–558. <https://doi.org/10.1038/nmat2753>.
- (5) Cai, W.; Moore, A. L.; Zhu, Y.; Li, X.; Chen, S.; Shi, L.; Ruoff, R. S. Thermal Transport in Suspended and Supported Monolayer Graphene Grown by Chemical Vapor Deposition. *Nano Letters* **2010**, *10* (5), 1645–1651. <https://doi.org/10.1021/nl9041966>.
- (6) Balandin, A. A. Thermal Properties of Graphene and Nanostructured Carbon Materials. *Nature Materials* **2011**, *10* (8), 569–581. <https://doi.org/10.1038/nmat3064>.
- (7) Shahil, K. M. F.; Balandin, A. A. Graphene-Multilayer Graphene Nanocomposites as Highly Efficient Thermal Interface Materials. *Nano Letters* **2012**, *12* (2), 861–867. <https://doi.org/10.1021/nl203906r>.
- (8) Goli, P.; Legedza, S.; Dhar, A.; Salgado, R.; Renteria, J.; Balandin, A. A. Graphene-Enhanced Hybrid Phase Change Materials for Thermal Management of Li-Ion Batteries. *Journal of Power Sources* **2014**, *248*, 37–43. <https://doi.org/10.1016/j.jpowsour.2013.08.135>.
- (9) Renteria, J.; Legedza, S.; Salgado, R.; Balandin, M. P.; Ramirez, S.; Saadah, M.; Kargar, F.; Balandin, A. A. Magnetically-Functionalized Self-Aligning Graphene Fillers for High-Efficiency Thermal Management Applications. *Materials & Design* **2015**, *88*, 214-221. <https://doi.org/10.1016/j.matdes.2015.08.135>.
- (10) Lewis, J. S.; Perrier, T.; Mohammadzadeh, A.; Kargar, F.; Balandin, A. A. Power Cycling and Reliability Testing of Epoxy-Based Graphene Thermal Interface Materials. *C – Journal of Carbon Research* **2020**, *6* (2), 26. <https://doi.org/10.3390/c6020026>.
- (11) Barani, Z.; Kargar, F.; Mohammadzadeh, A.; Naghibi, S.; Lo, C.; Rivera, B.; Balandin, A. A. Multifunctional Graphene Composites for Electromagnetic Shielding and Thermal Management at Elevated Temperatures. *Advanced Electronic Materials* **2020**, *6* (11), 2000520-undefined. <https://doi.org/10.1002aelm.202000520>.

(12) Barani, Z.; Mohammadzadeh, A.; Geremew, A.; Huang, C. Y.; Coleman, D.; Mangolini, L.; Kargar, F.; Balandin, A. A. Thermal Properties of the Binary-Filler Hybrid Composites with Graphene and Copper Nanoparticles. *Advanced Functional Materials* **2019**. <https://doi.org/10.1002/adfm.201904008>.

(13) Barani, Z.; Kargar, F.; Godziszewski, K.; Rehman, A.; Yashchyshyn, Y.; Rumyantsev, S.; Cywiński, G.; Knap, W.; Balandin, A. A. Graphene Epoxy-Based Composites as Efficient Electromagnetic Absorbers in the Extremely High-Frequency Band. *ACS Applied Materials and Interfaces* **2020**, *12* (25), 28635–28644. <https://doi.org/10.1021/acsami.0c06729>.

(14) Naghibi, S.; Kargar, F.; Wright, D.; Huang, C. Y. T.; Mohammadzadeh, A.; Barani, Z.; Salgado, R.; Balandin, A. A. Noncuring Graphene Thermal Interface Materials for Advanced Electronics. *Advanced Electronic Materials* **2020**, *1901303*. <https://doi.org/10.1002/aelm.201901303>.

(15) Kargar, F.; Barani, Z.; Salgado, R.; Debnath, B.; Lewis, J. S.; Aytan, E.; Lake, R. K.; Balandin, A. A. Thermal Percolation Threshold and Thermal Properties of Composites with High Loading of Graphene and Boron Nitride Fillers. *ACS Applied Materials and Interfaces* **2018**, *10* (43), 37555–37565. <https://doi.org/10.1021/acsami.8b16616>.

(16) Wang, Z.-G.; Lv, J.-C.; Zheng, Z.-L.; Du, J.-G.; Dai, K.; Lei, J.; Xu, L.; Xu, J.-Z.; Li, Z.-M. Highly Thermally Conductive Graphene-Based Thermal Interface Materials with a Bilayer Structure for Central Processing Unit Cooling. *ACS Applied Materials & Interfaces* **2021**. <https://doi.org/10.1021/acsami.1c01223>.

(17) Sudhindra, S.; Kargar, F.; Balandin, A. A. Noncured Graphene Thermal Interface Materials for High-Power Electronics: Minimizing the Thermal Contact Resistance. *Nanomaterials* **2021**, *11* (7), 1699. <https://doi.org/10.3390/nano11071699>.

(18) Lewis, J. S. Reduction of Device Operating Temperatures with Graphene-Filled Thermal Interface Materials. *C — Journal of Carbon Research* **2021**, *7* (3), 53. <https://doi.org/10.3390/c7030053>.

(19) Lv, L.; Dai, W.; Li, A.; Lin, C.-T. Graphene-Based Thermal Interface Materials: An Application-Oriented Perspective on Architecture Design. *Polymers* **2018**, *10* (11), 1201. <https://doi.org/10.3390/polym10111201>.

(20) Liu, C.; Yu, W.; Chen, C.; Xie, H.; Cao, B. Remarkably Reduced Thermal Contact Resistance of Graphene/Olefin Block Copolymer/Paraffin Form Stable Phase Change Thermal Interface Material. *International Journal of Heat and Mass Transfer* **2020**, *163*, 120393. <https://doi.org/10.1016/j.ijheatmasstransfer.2020.120393>.

(21) Cao, B.-Y.; Zou, J.-H.; Hu, G.-J.; Cao, G.-X. Enhanced Thermal Transport across Multilayer Graphene and Water by Interlayer Functionalization. *Applied Physics Letters* **2018**, *112* (4), 041603. <https://doi.org/10.1063/1.5018749>.

(22) Shtein, M.; Nadiv, R.; Buzaglo, M.; Regev, O. Graphene-Based Hybrid Composites for Efficient Thermal Management of Electronic Devices. *ACS Applied Materials & Interfaces* **2015**, *7* (42), 23725–23730. <https://doi.org/10.1021/acsami.5b07866>.

(23) Balandin, A. A. Phononics of Graphene and Related Materials. *ACS Nano* **2020**, *14* (5), 5170–5178. <https://doi.org/10.1021/acsnano.0c02718>.

(24) Fu, Y.; Hansson, J.; Liu, Y.; Chen, S.; Zehri, A.; Samani, M. K.; Wang, N.; Ni, Y.; Zhang, Y.; Zhang, Z.-B.; Wang, Q.; Li, M.; Lu, H.; Sledzinska, M.; Torres, C. M. S.; Volz, S.; Balandin, A. A.; Xu, X.; Liu, J. Graphene Related Materials for Thermal Management. *2D Materials* **2020**, *7* (1), 012001. <https://doi.org/10.1088/2053-1583/ab48d9>.

(25) Lewis, J. S.; Perrier, T.; Barani, Z.; Kargar, F.; Balandin, A. A. Thermal Interface Materials with Graphene Fillers: Review of the State of the Art and Outlook of Future Applications. *Nanotechnology* **2021**, *32* (14), 142003. <https://doi.org/10.1088/1361-6528/abc0c6>.

(26) Shtein, M.; Nadiv, R.; Buzaglo, M.; Kahil, K.; Regev, O. Thermally Conductive Graphene-Polymer Composites: Size, Percolation, and Synergy Effects. *Chemistry of Materials* **2015**, *27* (6), 2100–2106. <https://doi.org/10.1021/cm504550e>.

(27) Chun, K.-Y.; Oh, Y.; Rho, J.; Ahn, J.-H.; Kim, Y.-J.; Choi, H. R.; Baik, S. Highly Conductive, Printable and Stretchable Composite Films of Carbon Nanotubes and Silver. *Nature Nanotechnology* **2010**, *5* (12), 853–857. <https://doi.org/10.1038/nnano.2010.232>.

(28) Zhou, T.; Wang, X.; Liu, X.; Xiong, D. Improved Thermal Conductivity of Epoxy Composites Using a Hybrid Multi-Walled Carbon Nanotube/Micro-SiC Filler. *Carbon* **2010**, *48* (4), 1171–1176. <https://doi.org/10.1016/j.carbon.2009.11.040>.

(29) Ma, P.-C.; Liu, M.-Y.; Zhang, H.; Wang, S.-Q.; Wang, R.; Wang, K.; Wong, Y.-K.; Tang, B.-Z.; Hong, S.-H.; Paik, K.-W.; Kim, J.-K. Enhanced Electrical Conductivity of Nanocomposites Containing Hybrid Fillers of Carbon Nanotubes and Carbon Black. *ACS Applied Materials & Interfaces* **2009**, *1* (5), 1090–1096. <https://doi.org/10.1021/am9000503>.

(30) Wenyi Zhou; Caifeng Wang; Qunli An; Haiyan Ou. Thermal Properties of Heat Conductive Silicone Rubber Filled with Hybrid Fillers. *Journal of Composite Materials* **2008**, *42* (2), 173–187. <https://doi.org/10.1177/0021998307086184>.

(31) Devpura, A.; Phelan, P. E.; Prasher, R. S. Size Effects on the Thermal Conductivity of Polymers Laden with Highly Conductive Filler Particles. *Microscale Thermophysical Engineering* **2001**, *5* (3), 177–189. <https://doi.org/10.1080/108939501753222869>.

(32) Guoqing Zhang; Yanping Xia; Hui Wang; Yu Tao; Guoliang Tao; Shantung Tu; Haiping Wu. A Percolation Model of Thermal Conductivity for Filled Polymer Composites. *Journal of Composite Materials* **2010**, *44* (8), 963–970. <https://doi.org/10.1177/0021998309349690>.

(33) Debelak, B.; Lafdi, K. Use of Exfoliated Graphite Filler to Enhance Polymer Physical Properties. *Carbon* **2007**, *45* (9), 1727–1734. <https://doi.org/10.1016/j.carbon.2007.05.010>.

(34) Kim, H. S.; Bae, H. S.; Yu, J.; Kim, S. Y. Thermal Conductivity of Polymer Composites with the Geometrical Characteristics of Graphene Nanoplatelets. *Scientific Reports* **2016**, *6* (1), 26825. <https://doi.org/10.1038/srep26825>.

(35) Shen, X.; Wang, Z.; Wu, Y.; Liu, X.; He, Y.-B.; Kim, J.-K. Multilayer Graphene Enables Higher Efficiency in Improving Thermal Conductivities of Graphene/Epoxy Composites. *Nano Letters* **2016**, *16* (6), 3585–3593. <https://doi.org/10.1021/acs.nanolett.6b00722>.

(36) Jasnee, S.; Omar, G.; Othaman, S. S. C.; Masripan, N. A.; A. Hamid, H. Interface Thermal Resistance and Thermal Conductivity of Polymer Composites at Different Types, Shapes,

and Sizes of Fillers: A Review. *Polymer Composites* **2021**, *42* (6), 2629–2652. <https://doi.org/10.1002/pc.26029>.

(37) Moradi, S.; Calventus, Y.; Román, F.; Hutchinson, J. M. Achieving High Thermal Conductivity in Epoxy Composites: Effect of Boron Nitride Particle Size and Matrix-Filler Interface. *Polymers* **2019**, *11* (7), 1156. <https://doi.org/10.3390/polym11071156>.

(38) Zhou, W.-Y.; Qi, S.-H.; Zhao, H.-Z.; Liu, N.-L. Thermally Conductive Silicone Rubber Reinforced with Boron Nitride Particle. *Polymer Composites* **2007**, *28* (1), 23–28. <https://doi.org/10.1002/pc.20296>.

(39) Pawelski, C.; Kang, E.; Bakis, G.; Altstädt, V. Effect of Filler Type and Particle Size Distribution on Thermal Properties of Bimodal and Hybrid – BN/Boehmite-Filled EP-Novolac Composites. In *AIP Conference Proceedings*; 2019; p 050007. <https://doi.org/10.1063/1.5084826>.

(40) Tanimoto, M.; Yamagata, T.; Miyata, K.; Ando, S. Anisotropic Thermal Diffusivity of Hexagonal Boron Nitride-Filled Polyimide Films: Effects of Filler Particle Size, Aggregation, Orientation, and Polymer Chain Rigidity. *ACS Applied Materials & Interfaces* **2013**, *5* (10), 4374–4382. <https://doi.org/10.1021/am400615z>.

(41) Ashraf, M. A.; Peng, W.; Zare, Y.; Rhee, K. Y. Effects of Size and Aggregation/Agglomeration of Nanoparticles on the Interfacial/Interphase Properties and Tensile Strength of Polymer Nanocomposites. *Nanoscale Research Letters* **2018**, *13* (1), 214. <https://doi.org/10.1186/s11671-018-2624-0>.

(42) Mahanta, N. K.; Loos, M. R.; Manas Zlocozower, I.; Abramson, A. R. Graphite–Graphene Hybrid Filler System for High Thermal Conductivity of Epoxy Composites. *Journal of Materials Research* **2015**, *30* (7), 959–966. <https://doi.org/10.1557/jmr.2015.68>.

(43) Owais, M.; Zhao, J.; Imani, A.; Wang, G.; Zhang, H.; Zhang, Z. Synergetic Effect of Hybrid Fillers of Boron Nitride, Graphene Nanoplatelets, and Short Carbon Fibers for Enhanced Thermal Conductivity and Electrical Resistivity of Epoxy Nanocomposites. *Composites Part A: Applied Science and Manufacturing* **2019**, *117*, 11–22. <https://doi.org/10.1016/j.compositesa.2018.11.006>.

(44) Senturk, A. E.; Oktem, A. S.; Konukman, A. E. S. Investigation of Interfacial Thermal Resistance of Hybrid Graphene/Hexagonal Boron Nitride. *International Journal of Mechanics and Materials in Design* **2019**, *15* (4), 727–737. <https://doi.org/10.1007/s10999-018-09440-y>.

(45) Hernandez, Y.; Nicolosi, V.; Lotya, M.; Blighe, F. M.; Sun, Z.; De, S.; McGovern, I. T.; Holland, B.; Byrne, M.; Gun'Ko, Y. K.; Boland, J. J.; Niraj, P.; Duesberg, G.; Krishnamurthy, S.; Goodhue, R.; Hutchison, J.; Scardaci, V.; Ferrari, A. C.; Coleman, J. N. High-Yield Production of Graphene by Liquid-Phase Exfoliation of Graphite. *Nature Nanotechnology* **2008**, *3* (9), 563–568. <https://doi.org/10.1038/nnano.2008.215>.

(46) Lotya, M.; Hernandez, Y.; King, P. J.; Smith, R. J.; Nicolosi, V.; Karlsson, L. S.; Blighe, F. M.; De, S.; Wang, Z.; McGovern, I. T.; Duesberg, G. S.; Coleman, J. N. Liquid Phase Production of Graphene by Exfoliation of Graphite in Surfactant/Water Solutions. *Journal of the American Chemical Society* **2009**, *131* (10), 3611–3620. <https://doi.org/10.1021/ja807449u>.

(47) Nicolosi, V.; Chhowalla, M.; Kanatzidis, M. G.; Strano, M. S.; Coleman, J. N. Liquid Exfoliation of Layered Materials. *Science* **2013**, *340* (6139), 1226419–1226419. <https://doi.org/10.1126/science.1226419>.

(48) Tao, H.; Zhang, Y.; Gao, Y.; Sun, Z.; Yan, C.; Texter, J. Scalable Exfoliation and Dispersion of Two-Dimensional Materials – an Update. *Physical Chemistry Chemical Physics* **2017**, *19* (2), 921–960. <https://doi.org/10.1039/C6CP06813H>.

(49) Bonaccorso, F.; Bartolotta, A.; Coleman, J. N.; Backes, C. 2D-Crystal-Based Functional Inks. *Advanced Materials* **2016**, *28* (29), 6136–6166. <https://doi.org/10.1002/adma.201506410>.

(50) Backes, C.; Szydłowska, B. M.; Harvey, A.; Yuan, S.; Vega-Mayoral, V.; Davies, B. R.; Zhao, P.; Hanlon, D.; Santos, E. J. G.; Katsnelson, M. I.; Blau, W. J.; Gadermaier, C.; Coleman, J. N. Production of Highly Monolayer Enriched Dispersions of Liquid-Exfoliated Nanosheets by Liquid Cascade Centrifugation. *ACS Nano* **2016**, *10* (1), 1589–1601. <https://doi.org/10.1021/acsnano.5b07228>.

(51) Backes, C.; Paton, K. R.; Hanlon, D.; Yuan, S.; Katsnelson, M. I.; Houston, J.; Smith, R. J.; McCloskey, D.; Donegan, J. F.; Coleman, J. N. Spectroscopic Metrics Allow in Situ Measurement of Mean Size and Thickness of Liquid-Exfoliated Few-Layer Graphene Nanosheets. *Nanoscale* **2016**, *8* (7), 4311–4323. <https://doi.org/10.1039/C5NR08047A>.

(52) Backes, C.; Campi, D.; Szydlowska, B. M.; Synnatschke, K.; Ojala, E.; Rashvand, F.; Harvey, A.; Griffin, A.; Sofer, Z.; Marzari, N.; Coleman, J. N.; O'Regan, D. D. Equipartition of Energy Defines the Size–Thickness Relationship in Liquid-Exfoliated Nanosheets. *ACS Nano* **2019**, *13* (6), 7050–7061. <https://doi.org/10.1021/acsnano.9b02234>.

(53) Nika, D. L.; Ghosh, S.; Pokatilov, E. P.; Balandin, A. A. Lattice Thermal Conductivity of Graphene Flakes: Comparison with Bulk Graphite. *Applied Physics Letters* **2009**, *94* (20), 203103. <https://doi.org/10.1063/1.3136860>.

(54) Balandin, A. A.; Ghosh, S.; Nika, D. L.; Pokatilov, E. P. Thermal Conduction in Suspended Graphene Layers. *Fullerenes, Nanotubes and Carbon Nanostructures* **2010**, *18* (4–6), 474–486. <https://doi.org/10.1080/1536383X.2010.487785>.

(55) Nika, D. L.; Askerov, A. S.; Balandin, A. A. Anomalous Size Dependence of the Thermal Conductivity of Graphene Ribbons. *Nano Letters* **2012**, *12* (6), 3238–3244. <https://doi.org/10.1021/nl301230g>.

(56) Nika, D. L.; Balandin, A. A. Two-Dimensional Phonon Transport in Graphene. *Journal of Physics: Condensed Matter* **2012**, *24* (23), 233203. <https://doi.org/10.1088/0953-8984/24/23/233203>.

(57) Balandin, A. A.; Nika, D. L. Phononics in Low-Dimensional Materials. *Materials Today* **2012**, *15* (6), 266–275. [https://doi.org/10.1016/S1369-7021\(12\)70117-7](https://doi.org/10.1016/S1369-7021(12)70117-7).

(58) Nika, D. L.; Pokatilov, E. P.; Askerov, A. S.; Balandin, A. A. Phonon Thermal Conduction in Graphene: Role of Umklapp and Edge Roughness Scattering. *Physical Review B* **2009**, *79* (15), 155413. <https://doi.org/10.1103/PhysRevB.79.155413>.

(59) Ferrari, A. C.; Meyer, J. C.; Scardaci, V.; Casiraghi, C.; Lazzeri, M.; Mauri, F.; Piscanec, S.; Jiang, D.; Novoselov, K. S.; Roth, S.; Geim, A. K. Raman Spectrum of Graphene and

Graphene Layers. *Physical Review Letters* **2006**, *97* (18), 187401. <https://doi.org/10.1103/PhysRevLett.97.187401>.

(60) Calizo, I.; Balandin, A. A.; Bao, W.; Miao, F.; Lau, C. N. Temperature Dependence of the Raman Spectra of Graphene and Graphene Multilayers. *Nano Letters* **2007**, *7* (9), 2645–2649. <https://doi.org/10.1021/nl071033g>.

(61) Calizo, I.; Teweldebrhan, D.; Bao, W.; Miao, F.; Lau, C. N.; Balandin, A. A. Spectroscopic Raman Nanometrology of Graphene and Graphene Multilayers on Arbitrary Substrates. *Journal of Physics: Conference Series* **2008**, *109*, 012008. <https://doi.org/10.1088/1742-6596/109/1/012008>.

(62) Gupta, A.; Chen, G.; Joshi, P.; Tadigadapa, S.; Eklund. Raman Scattering from High-Frequency Phonons in Supported n -Graphene Layer Films. *Nano Letters* **2006**, *6* (12), 2667–2673. <https://doi.org/10.1021/nl061420a>.

(63) Graf, D.; Molitor, F.; Ensslin, K.; Stampfer, C.; Jungen, A.; Hierold, C.; Wirtz, L. Spatially Resolved Raman Spectroscopy of Single- and Few-Layer Graphene. *Nano Letters* **2007**, *7* (2), 238–242. <https://doi.org/10.1021/nl061702a>.

(64) Malard, L. M.; Pimenta, M. A.; Dresselhaus, G.; Dresselhaus, M. S. Raman Spectroscopy in Graphene. *Physics Reports* **2009**, *473* (5–6), 51–87. <https://doi.org/10.1016/j.physrep.2009.02.003>.

(65) Khan, U.; O'Neill, A.; Porwal, H.; May, P.; Nawaz, K.; Coleman, J. N. Size Selection of Dispersed, Exfoliated Graphene Flakes by Controlled Centrifugation. *Carbon* **2012**, *50* (2), 470–475. <https://doi.org/10.1016/j.carbon.2011.09.001>.

(66) Parvizi, F.; Teweldebrhan, D.; Ghosh, S.; Calizo, I.; Balandin, A. A.; Zhu, H.; Abbaschian, R. Properties of Graphene Produced by the High Pressure–High Temperature Growth Process. *Micro & Nano Letters* **2008**, *3* (1), 29. <https://doi.org/10.1049/mnl:20070074>.

(67) Teweldebrhan, D.; Balandin, A. A. Modification of Graphene Properties Due to Electron-Beam Irradiation. *Applied Physics Letters* **2009**, *94* (1), 013101. <https://doi.org/10.1063/1.3062851>.

(68) Silva, D. L.; Campos, J. L. E.; Fernandes, T. F. D.; Rocha, J. N.; Machado, L. R. P.; Soares, E. M.; Miquita, D. R.; Miranda, H.; Rabelo, C.; Vilela Neto, O. P.; Jorio, A.; Cançado, L. G. Raman Spectroscopy Analysis of Number of Layers in Mass-Produced Graphene Flakes. *Carbon* **2020**, *161*, 181–189. <https://doi.org/10.1016/j.carbon.2020.01.050>.

(69) Goel, N.; Anoop, T. K.; Bhattacharya, A.; Cervantes, J. A.; Mongia, R. K.; Machiroutu, S. v.; Lin, H.-L.; Huang, Y.-C.; Fan, K.-C.; Denq, B.-L.; Liu, C.-H.; Lin, C.-H.; Tien, C.-W.; Pan, J.-H. Technical Review of Characterization Methods for Thermal Interface Materials (TIM). In *2008 11th IEEE Intersociety Conference on Thermal and Thermomechanical Phenomena in Electronic Systems*; 2008; pp 248–258. <https://doi.org/10.1109/ITHERM.2008.4544277>.

(70) Prasher, R. Thermal Interface Materials: Historical Perspective, Status, and Future Directions. *Proceedings of the IEEE* **2006**, *94* (8), 1571–1586. <https://doi.org/10.1109/JPROC.2006.879796>.

(71) Shahil, K. M. F.; Balandin, A. A. Thermal Properties of Graphene and Multilayer Graphene: Applications in Thermal Interface Materials. *Solid State Communications* **2012**, *152* (15), 1331–1340. <https://doi.org/10.1016/j.ssc.2012.04.034>.

(72) Prasher, R. S.; Shipley, J.; Prstic, S.; Koning, P.; Wang, J. Thermal Resistance of Particle Laden Polymeric Thermal Interface Materials. *Journal of Heat Transfer* **2003**, *125* (6), 1170–1177. <https://doi.org/10.1115/1.1621893>.

(73) Prasher, R. S.; Matayabas, J. C. Thermal Contact Resistance of Cured Gel Polymeric Thermal Interface Material. *Thermomechanical Phenomena in Electronic Systems - Proceedings of the Intersociety Conference* **2004**, *1* (4), 28–35. <https://doi.org/10.1109/therm.2004.1319150>.

(74) Gwinn, J. P.; Webb, R. L. Performance and Testing of Thermal Interface Materials. In *Microelectronics Journal*; 2003; Vol. 34, pp 215–222. [https://doi.org/10.1016/S0026-2692\(02\)00191-X](https://doi.org/10.1016/S0026-2692(02)00191-X).

(75) Skuriat, R.; Li, J. F.; Agyakwa, P. A.; Mattey, N.; Evans, P.; Johnson, C. M. Degradation of Thermal Interface Materials for High-Temperature Power Electronics Applications.

Microelectronics Reliability **2013**, *53* (12), 1933–1942.
<https://doi.org/10.1016/j.microrel.2013.05.011>.

(76) Hurley, S.; Cann, P. M.; Spikes, H. A. Lubrication and Reflow Properties of Thermally Aged Greases. *Tribology Transactions* **2000**, *43* (2), 221–228. <https://doi.org/10.1080/10402000008982332>.

(77) Mortezaei, M.; Farzi, G.; Kalaei, M. R.; Zabihpoor, M. Evaluation of Interfacial Layer Properties in the Polystyrene/Silica Nanocomposite. *Journal of Applied Polymer Science* **2011**, *119* (4), 2039–2047. <https://doi.org/10.1002/app.32902>.

(78) Mortezaei, M.; Famili, M. H. N.; Kokabi, M. Influence of the Particle Size on the Viscoelastic Glass Transition of Silica-Filled Polystyrene. *Journal of Applied Polymer Science* **2010**, *115* (2), 969–975. <https://doi.org/10.1002/app.31048>.

(79) Wang, J. Shear Modulus Measurement for Thermal Interface Materials in Flip Chip Packages. *IEEE Transactions on Components and Packaging Technologies* **2006**, *29* (3), 610–617. <https://doi.org/10.1109/TCAPT.2006.880505>.

(80) Iisaka, K.; Shibayama, K. Effect of Filler Particle Size on Dynamic Mechanical Properties of Poly(Methyl Methacrylate). *Journal of Applied Polymer Science* **1978**, *22* (5), 1321–1330. <https://doi.org/10.1002/app.1978.070220513>.

(81) Wu, X.; Lin, T. F.; Tang, Z. H.; Guo, B. C.; Huang, G. S. Natural Rubber/Graphene Oxide Composites: Effect of Sheet Size on Mechanical Properties and Strain-Induced Crystallization Behavior. *Express Polymer Letters* **2015**, *9* (8), 672–685. <https://doi.org/10.3144/expresspolymlett.2015.63>.

(82) Hristov, V.; Vlachopoulos, J. Effects of Polymer Molecular Weight and Filler Particle Size on Flow Behavior of Wood Polymer Composites. *Polymer Composites* **2008**, *29* (8), 831–839. <https://doi.org/10.1002/pc.20455>.

(83) Osman, M. A.; Atallah, A. Effect of the Particle Size on the Viscoelastic Properties of Filled Polyethylene. *Polymer* **2006**, *47* (7), 2357–2368. <https://doi.org/10.1016/j.polymer.2006.01.085>.

(84) McGrath, L. M.; Parnas, R. S.; King, S. H.; Schroeder, J. L.; Fischer, D. A.; Lenhart, J. L. Investigation of the Thermal, Mechanical, and Fracture Properties of Alumina–Epoxy Composites. *Polymer* **2008**, *49* (4), 999–1014. <https://doi.org/10.1016/j.polymer.2007.12.014>.

(85) Prasher, R. S.; Koning, P.; Shipley, J.; Devpura, A. Dependence of Thermal Conductivity and Mechanical Rigidity of Particle-Laden Polymeric Thermal Interface Material on Particle Volume Fraction. *Journal of Electronic Packaging* **2003**, *125* (3), 386–391. <https://doi.org/10.1115/1.1602703>.

(86) Huang, Z.; Wu, W.; Drummer, D.; Liu, C.; Wang, Y.; Wang, Z. Enhanced the Thermal Conductivity of Polydimethylsiloxane via a Three-Dimensional Hybrid Boron Nitride@Silver Nanowires Thermal Network Filler. *Polymers* **2021**, *13* (2), 248. <https://doi.org/10.3390/polym13020248>.

(87) Mark, James. E. *Polymer Data Handbook*; Oxford University Press: New York, 1999.

(88) Zhao, Y.-H.; Zhang, Y.-F.; Bai, S.-L. High Thermal Conductivity of Flexible Polymer Composites Due to Synergistic Effect of Multilayer Graphene Flakes and Graphene Foam. *Composites Part A: Applied Science and Manufacturing* **2016**, *85*, 148–155. <https://doi.org/10.1016/j.compositesa.2016.03.021>.

(89) Bae, M.-H.; Li, Z.; Aksamija, Z.; Martin, P. N.; Xiong, F.; Ong, Z.-Y.; Knezevic, I.; Pop, E. Ballistic to Diffusive Crossover of Heat Flow in Graphene Ribbons. *Nature Communications* **2013**, *4* (1), 1734. <https://doi.org/10.1038/ncomms2755>.

(90) Kanari, K. Thermal Conductivity of Composite Materials (In Japanese). *Kobunshi* **1977**, *26* (8), 557–561. <https://doi.org/10.1295/kobunshi.26.557>.

(91) Bruggeman, D. A. G. Berechnung Verschiedener Physikalischer Konstanten von Heterogenen Substanzen. *Annals of Physics* **1935**, *24*, 636–679.

(92) Drozdov, A. D.; deClaville Christiansen, J. Modeling Thermal Conductivity of Highly Filled Polymer Composites. *Polymer Engineering & Science* **2019**, *59* (10), 2174–2179. <https://doi.org/10.1002/pen.25220>.

(93) Kargar, F.; Barani, Z.; Balinskiy, M.; Magana, A. S.; Lewis, J. S.; Balandin, A. A. Dual-Functional Graphene Composites for Electromagnetic Shielding and Thermal Management. *Advanced Electronic Materials* **2019**, *5* (1). <https://doi.org/10.1002aelm.201800558>.

(94) Raza, M. A.; Westwood, A.; Brown, A.; Hondow, N.; Stirling, C. Characterisation of Graphite Nanoplatelets and the Physical Properties of Graphite Nanoplatelet/Silicone Composites for Thermal Interface Applications. *Carbon* **2011**, *49* (13), 4269–4279. <https://doi.org/10.1016/j.carbon.2011.06.002>.

(95) Raza, M. A.; Westwood, A. V. K.; Brown, A. P.; Stirling, C. Texture, Transport and Mechanical Properties of Graphite Nanoplatelet/Silicone Composites Produced by Three Roll Mill. *Composites Science and Technology* **2012**, *72* (3), 467–475. <https://doi.org/10.1016/j.compscitech.2011.12.010>.

(96) Paton, K. R.; Varrla, E.; Backes, C.; Smith, R. J.; Khan, U.; O'Neill, A.; Boland, C.; Lotya, M.; Istrate, O. M.; King, P.; Higgins, T.; Barwick, S.; May, P.; Puczkarski, P.; Ahmed, I.; Moebius, M.; Pettersson, H.; Long, E.; Coelho, J.; O'Brien, S. E.; McGuire, E. K.; Sanchez, B. M.; Duesberg, G. S.; McEvoy, N.; Pennycook, T. J.; Downing, C.; Crossley, A.; Nicolosi, V.; Coleman, J. N. Scalable Production of Large Quantities of Defect-Free Few-Layer Graphene by Shear Exfoliation in Liquids. *Nature Materials* **2014**, *13* (6), 624–630. <https://doi.org/10.1038/nmat3944>.

(97) Synnatschke, K.; Cieslik, P. A.; Harvey, A.; Castellanos-Gomez, A.; Tian, T.; Shih, C.-J.; Chernikov, A.; Santos, E. J. G.; Coleman, J. N.; Backes, C. Length- and Thickness-Dependent Optical Response of Liquid-Exfoliated Transition Metal Dichalcogenides. *Chemistry of Materials* **2019**, *31* (24), 10049–10062. <https://doi.org/10.1021/acs.chemmater.9b02905>.